



Aalborg Universitet

AALBORG UNIVERSITY
DENMARK

Numerical Modeling of a Spherical Array of Monopoles Using FDTD Method

Franek, Ondrej; Pedersen, Gert Frølund; Andersen, Jørgen Bach

Published in:
IEEE Transactions on Antennas and Propagation

DOI (link to publication from Publisher):
[10.1109/TAP.2006.877202](https://doi.org/10.1109/TAP.2006.877202)

Publication date:
2006

Document Version
Accepted author manuscript, peer reviewed version

[Link to publication from Aalborg University](#)

Citation for published version (APA):
Franek, O., Pedersen, G. F., & Andersen, J. B. (2006). Numerical Modeling of a Spherical Array of Monopoles Using FDTD Method. *IEEE Transactions on Antennas and Propagation*, 54(7), 1952-1963.
<https://doi.org/10.1109/TAP.2006.877202>

General rights

Copyright and moral rights for the publications made accessible in the public portal are retained by the authors and/or other copyright owners and it is a condition of accessing publications that users recognise and abide by the legal requirements associated with these rights.

- Users may download and print one copy of any publication from the public portal for the purpose of private study or research.
- You may not further distribute the material or use it for any profit-making activity or commercial gain
- You may freely distribute the URL identifying the publication in the public portal -

Take down policy

If you believe that this document breaches copyright please contact us at vbn@aub.aau.dk providing details, and we will remove access to the work immediately and investigate your claim.

Numerical Modeling of a Spherical Array of Monopoles Using FDTD Method

Ondřej Franek, *Member, IEEE*, Gert Frølund Pedersen, and Jørgen Bach Andersen, *Life Fellow, IEEE*

Abstract—In this paper, the spherical-coordinate finite-difference time-domain (FDTD) method is applied to numerical analysis of phased array of monopoles distributed over a sphere. Outer boundary of the given problem is modeled by accurate spherical-coordinate anisotropic perfectly matched layer (PML). The problem of increased cell aspect ratio near the sphere poles causing degradation of results is solved by dispersion optimization through artificial anisotropy. The accuracy of the approach is verified by comparing a model case with an exact solution. Finally, radiation patterns obtained by frequency-domain near-to-far-field transform and s-parameters of the array elements are presented and validated by comparing with measurement data.

Index Terms—FDTD methods, Spherical coordinates, Spherical antennas, Antenna arrays, Ultrawideband technology

I. INTRODUCTION

WITH the advent of the new generation of mobile communication technology, more attention is given to proper modeling of the channel characteristics. This raises a need for antennas, specially designed for measurement campaigns and capable of determining the direction of arrival (DOA) and polarization of incoming wave, impinging on the antenna from virtually whole exterior space. Commonly used planar phased arrays can satisfactorily resolve DOA only in a limited angular region, apart from the fact that the polarization properties of the signal remains usually unknown. Real omnidirectional antennas should provide total independence of the beam shape when steered over all possible angles of incidence. The described goal is closely approximated by spherical phased arrays.

Early theoretical work on spherical arrays can be found in [1]–[4]. In practical implementations, different numbers of various element types distributed over a sphere surface have been used. The 120-element constellation with conformal circular patches was mentioned in [5]. Another version of spherical array, with turnstile antennas as array elements, is numerically analyzed and discussed in [6]. In the measurement system described in [7], 32 dual-polarized rectangular microstrip patches are utilized. A phased array of 36 and 54 spiral antennas randomly dispersed over a sphere has been proposed in [8]. Finally, in [9], a spherical dodecahedral distribution of twelve monopoles is designed and investigated.

Monopoles are also used in the present antenna as they offer good broadband and even ultrawideband (UWB) performance

and, at the same time, they are relatively easy to implement. A total number of 32 elements are positioned on a metallic sphere in quasi-uniform pattern, yielding the lowest possible sidelobe level given by optimization. The antenna was designed for operating in frequency range 3–6 GHz, with a view to receiving signals from arbitrary direction and with arbitrary polarization.

In the present paper, numerical analysis of the above described spherical phased array is presented. The well-known and established finite-difference time-domain (FDTD) method [10] was chosen to accomplish the task. The FDTD method has previously proven to be an efficient and straightforward technique for analysis of several types of antennas. Although the preceding works on spherical arrays ([8], [9]) utilized the method of moments (MoM), the FDTD can be advantageous in cases when dielectric materials are present in the structure.

When applying the FDTD method to curved structures such as the spherical array, one has to face the problem of proper incorporation of the boundaries into the FDTD algorithm, as the inaccuracy inherent in staircasing approximation is well known. One possible solution is to employ some type of subcell technique [11]. The present authors decided to take advantage of the spherical coordinate system, which naturally conforms to the geometry of the submitted problem. The spherical coordinate FDTD concept was first introduced in [12]. Later, it was successfully used for analysis of conical antennas [13], spherical cavities [14], and recently also to extremely low frequency propagation in the Earth-ionosphere waveguide [15]. Application of the spherical-coordinate FDTD method to numerical analysis of spherical array antennas is new and has not appeared in the literature before. In addition, the monopoles were modeled by modified thin-rod approximation technique [16], which was adapted to the spherical coordinate system.

The remaining part of the paper is organized as follows. First of all, the investigated spherical antenna is briefly introduced in section II. In section III, the spherical-coordinate finite-difference time-domain method is described. Section IV presents the process of transformation of near-field response to far field, while the modeling of particular monopoles and their feeding and loading is reported in section V. In section VI, the numerical results are compared with exact solution of simplified problem and with measurement data of the physical realization of the spherical array. Finally, the results are discussed in section VII.

O. Franek is with the Institute of Radio Electronics, Brno University of Technology, CZ-612 00 Brno, Czech Republic (e-mail: franek@feec.vutbr.cz)

G. F. Pedersen and J. B. Andersen are with the Antennas and Propagation Division, Aalborg University, DK-9220 Aalborg Øst, Denmark (e-mail: gfp@kom.auc.dk, jba@cpk.auc.dk)

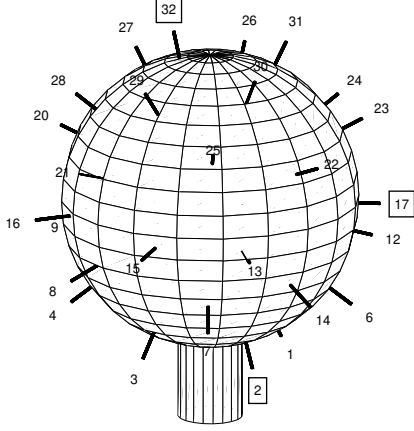


Fig. 1. The spherical array antenna with numbered monopoles—emphasized are the monopoles for which radiation patterns in Figs. 8–12 are plotted

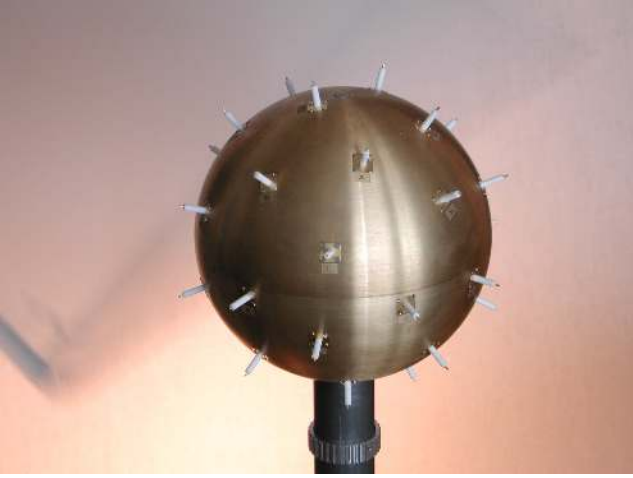


Fig. 2. The spherical array antenna: the realization

II. SPHERICAL ARRAY OF MONOPOLES

Design of the antenna modeled in this paper was motivated by highest possible flexibility in steering the beam while preserving wide frequency range of operation. The antenna (Figs. 1, 2, 19) is formed by a brass sphere of diameter 195 mm mounted on a metallic rod of diameter 42 mm. The rod serves as a mechanical support as well as a lead for cables feeding the array elements. The array aperture consists of 32 monopoles spread over the spherical surface in a quasi-uniform pattern. Such homogenous distribution of the monopoles, when appropriately phased, supports radiation in arbitrary direction with arbitrary polarization.

The monopoles are formed by teflon coated stubs at the backsides of SMA connectors mounted inward the sphere. Their dimensions are given in section V.

III. SPHERICAL COORDINATE FDTD

The computational domain for FDTD is subdivided into $I \times J \times K$ Yee-type volume cells [17], extending outwards from the metallic sphere of radius r_0 . The arrangement of the

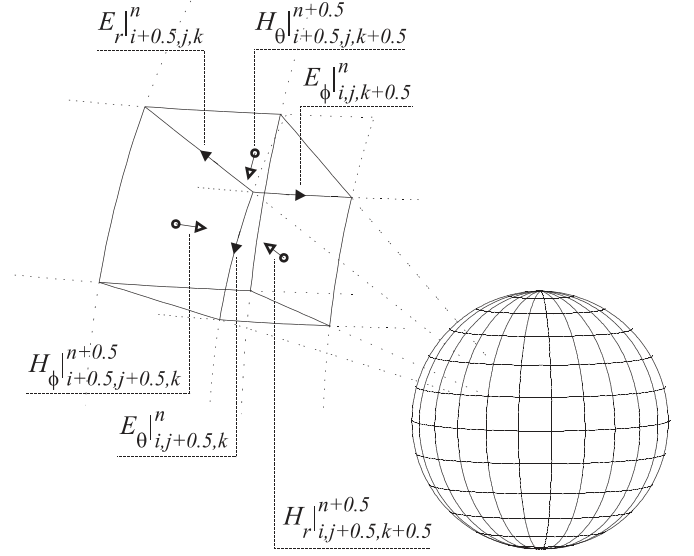


Fig. 3. Yee cell in spherical coordinate system

field components in the cell is shown in Fig. 3. The spherical coordinates of the field components, cell edges and cell faces are $r|_i = r_0 + i\Delta r$, $\theta|_j = j\Delta\theta$ and $\phi|_k = k\Delta\phi$, where $i = 0, \dots, I-1$, $j = 0, \dots, J-1$ and $k = 0, \dots, K-1$ are the cell indices and Δr , $\Delta\theta = \pi/J$, $\Delta\phi = 2\pi/K$ are spatial lattice steps in particular directions. In the time domain, the field components are distributed in usual leap-frog manner, at time points $t|_n = n\Delta t$ with temporal step Δt .

When approaching to the sphere poles, the excentricity of the FDTD cells is increasing. This puts a constraint on the time step, which is a function of dimension of the smallest cell in the grid. In addition, the cell shape affects the propagation characteristics of the wave in the lattice due to numerical dispersion and anisotropy. To reduce this effect, correction coefficients for material permittivity and permeability tensors are computed for each field component. The procedure was described thoroughly in [18], yielding local parameters ε_x , ε_y , ε_z and μ_x , μ_y , μ_z for multiplication with intrinsic material constants. However, these parameters can be derived for single frequency only. Although in [18] it is recommended to use the lowest frequency of the range of interest, the present scheme was tuned to optimum dispersion on the highest frequency, 6 GHz, as this turned out to be the best choice.

The update equations for the field components originate from Faraday's and Ampere's laws in integral form. After discretization in terms of Fig. 1 we obtain three local vector components for both electric and magnetic field components:

$$\begin{aligned}
 E_r|_{i+0.5,j,k}^{n+1} &= E_r|_{i+0.5,j,k}^n + \frac{\Delta t}{\varepsilon_r|_{i+0.5,j,k} A_r|_{i+0.5,j}} \\
 &\times \left[\left(H_{\theta}|_{i+0.5,j,k-0.5}^{n+0.5} - H_{\theta}|_{i+0.5,j,k+0.5}^{n+0.5} \right) l_{\theta}|_{i+0.5} \right. \\
 &\quad + H_{\phi}|_{i+0.5,j+0.5,k}^{n+0.5} l_{\phi}|_{i+0.5,j+0.5} \\
 &\quad \left. - H_{\phi}|_{i+0.5,j-0.5,k}^{n+0.5} l_{\phi}|_{i+0.5,j-0.5} \right] \quad (1)
 \end{aligned}$$

$$E_{\theta}|_{i,j+0.5,k}^{n+1} = E_{\theta}|_{i,j+0.5,k}^n + \frac{\Delta t}{\varepsilon_{\theta}|_{i,j+0.5,k} A_{\theta}|_{i,j+0.5}} \times \left[\left(H_r|_{i,j+0.5,k+0.5}^{n+0.5} - H_r|_{i,j+0.5,k-0.5}^{n+0.5} \right) l_r - H_{\phi}|_{i+0.5,j+0.5,k}^{n+0.5} l_{\phi}|_{i+0.5,j+0.5} + H_{\phi}|_{i-0.5,j+0.5,k}^{n+0.5} l_{\phi}|_{i-0.5,j+0.5} \right] \quad (2)$$

$$E_{\phi}|_{i,j,k+0.5}^{n+1} = E_{\phi}|_{i,j,k+0.5}^n + \frac{\Delta t}{\varepsilon_{\phi}|_{i,j,k+0.5} A_{\phi}|_i} \times \left[\left(H_r|_{i,j-0.5,k+0.5}^{n+0.5} - H_r|_{i,j+0.5,k+0.5}^{n+0.5} \right) l_r + H_{\theta}|_{i+0.5,j,k+0.5}^{n+0.5} l_{\theta}|_{i+0.5} - H_{\theta}|_{i-0.5,j,k+0.5}^{n+0.5} l_{\theta}|_{i-0.5} \right] \quad (3)$$

$$H_r|_{i,j+0.5,k+0.5}^{n+0.5} = H_r|_{i,j+0.5,k+0.5}^{n-0.5} - \frac{\Delta t / \mu_r|_{i,j+0.5,k+0.5}}{A_r|_{i,j+0.5}} \times \left[\left(E_{\theta}|_{i,j+0.5,k}^n - E_{\theta}|_{i,j+0.5,k+1}^n \right) l_{\theta}|_i + E_{\phi}|_{i,j+1,k+0.5}^n l_{\phi}|_{i,j+1} - E_{\phi}|_{i,j,k+0.5}^n l_{\phi}|_{i,j} \right] \quad (4)$$

$$H_{\theta}|_{i+0.5,j,k+0.5}^{n+0.5} = H_{\theta}|_{i+0.5,j,k+0.5}^{n-0.5} - \frac{\Delta t / \mu_{\theta}|_{i+0.5,j,k+0.5}}{A_{\theta}|_{i+0.5,j}} \times \left[\left(E_r|_{i+0.5,j,k+1}^n - E_r|_{i+0.5,j,k}^n \right) l_r - E_{\phi}|_{i+1,j,k+0.5}^n l_{\phi}|_{i+1,j} + E_{\phi}|_{i,j,k+0.5}^n l_{\phi}|_{i,j} \right] \quad (5)$$

$$H_{\phi}|_{i+0.5,j+0.5,k}^{n+0.5} = H_{\phi}|_{i+0.5,j+0.5,k}^{n-0.5} - \frac{\Delta t / \mu_{\phi}|_{i+0.5,j+0.5,k}}{A_{\phi}|_{i+0.5}} \times \left[\left(E_r|_{i+0.5,j,k}^n - E_r|_{i+0.5,j+1,k}^n \right) l_r + E_{\theta}|_{i+1,j+0.5,k}^n l_{\theta}|_{i+1} - E_{\theta}|_{i,j+0.5,k}^n l_{\theta}|_i \right] \quad (6)$$

In the above expressions, the lengths of the cell edges are

$$l_r = \Delta r \quad (7)$$

$$l_{\theta}|_i = r|_i \Delta \theta \quad (8)$$

$$l_{\phi}|_{i,j} = r|_i \Delta \phi \sin \theta|_j \quad (9)$$

while the cell face areas can be computed as

$$A_r|_{i,j} = 2r^2|_i \Delta \phi \sin(\Delta \theta / 2) \sin \theta|_j \quad (10)$$

$$A_{\theta}|_{i,j} = r|_i \Delta r \Delta \phi \sin \theta|_j \quad (11)$$

$$A_{\phi}|_i = r|_i \Delta r \Delta \theta. \quad (12)$$

The indices i, j relate to the center points of either the edges and faces.

The material parameters are defined

$$\varepsilon_{\zeta}|_{i,j,k} = \varepsilon_0 \varepsilon_{\text{rel}}|_{i,j,k} \varepsilon_{\nu}|_{i,j} \quad (13)$$

$$\mu_{\zeta}|_{i,j,k} = \mu_0 \mu_{\text{rel}}|_{i,j,k} \mu_{\nu}|_{i,j} \quad (14)$$

where $\zeta = r, \theta, \phi$ and $\nu = x, y, z$, respectively. Here, ε_0, μ_0 are the permittivity and permeability of vacuum and $\varepsilon_{\text{rel}}|_{i,j,k}, \mu_{\text{rel}}|_{i,j,k}$ represent the relative permittivity and permeability of the material being modeled, in points given by indices i, j, k . The parameters $\varepsilon_{\nu}|_{i,j}$ and $\mu_{\nu}|_{i,j}$ are local numerical dispersion and anisotropy correction coefficients defined according to [18].

The inner boundary of the grid is formed by the metallic surface of the sphere, which serves as a ground plane for radiators of the phased array. This surface is modeled by perfect electric conductor, where the tangential electric fields are forced to zero, $E_{\theta}|_{0,j,k}^n = E_{\phi}|_{0,j,k}^n = 0$. On the outer boundary, the mesh is terminated by anisotropic PML in spherical coordinate system [19]. The conductivity profile of the PML layer is polynomial of fourth order with maximum conductivity taken from [20].

Concerning the sphere poles, the surface areas $A_r|_{i,0}$ and $A_{\theta}|_{i,0}$ are equal to zero, which leads to singularities in expressions (1) and (5). Consequently, the radial electric field component at the north pole ($j = 0$) has to be updated in different way

$$E_r|_{i+0.5,0,k}^{n+1} = E_r|_{i+0.5,0,k}^n + \frac{\Delta t l_{\phi}|_{i+0.5,0.5}}{\varepsilon_r|_{i+0.5,0,k} A_{\text{cap}}|_{i+0.5}} \times \sum_{k'=0}^{K-1} H_{\phi}|_{i+0.5,0.5,k'}^{n+0.5} \quad (15)$$

where $A_{\text{cap}}|_i = 2\pi r^2|_i (1 - \cos(\Delta \theta / 2))$ is the area of the pole cap. The update equation for the south pole ($j = J$) is similar, only with opposite sign of the sum on the right-hand side. The magnetic field components $H_{\theta}|_{i+0.5,0,k+0.5}^{n+0.5}, H_{\phi}|_{i+0.5,J,k+0.5}^{n+0.5}$ are not updated as they are not needed at all and the electric fields $E_{\phi}|_{i,0,k+0.5}^n, E_{\phi}|_{i,J,k+0.5}^n$, although not singular, are kept zero. The remaining field components follow the standard formulas (1)–(6).

Finally, periodic boundary conditions are employed to link both ends of the spherical grid in azimuthal direction. Since $H_r|_{i,j+0.5,K-0.5}^{n+0.5}$ and $H_{\theta}|_{i+0.5,j,K-0.5}^{n+0.5}$ depend on electric fields which are not part of the lattice, these must be additionally defined as

$$E_r|_{i+0.5,j,K}^n = E_r|_{i+0.5,j,0}^n \quad (16)$$

$$E_{\theta}|_{i,j+0.5,K}^n = E_{\theta}|_{i,j+0.5,0}^n \quad (17)$$

Similarly, $E_r|_{i+0.5,j,0}^{n+1}$ and $E_{\theta}|_{i,j+0.5,0}^{n+1}$ are computed using values

$$H_r|_{i,j+0.5,-0.5}^{n+0.5} = H_r|_{i,j+0.5,K-0.5}^{n+0.5} \quad (18)$$

$$H_{\theta}|_{i+0.5,j,-0.5}^{n+0.5} = H_{\theta}|_{i+0.5,j,K-0.5}^{n+0.5} \quad (19)$$

from the opposite end of the lattice.

IV. NEAR-FIELD TO FAR-FIELD TRANSFORM

The radiation pattern of the antenna is deduced by transforming the field responses inside the computational domain to the far-field region. This is done by integrating the equivalent surface electric and magnetic currents over the spherical surface, so that all possible sources are inside the surface.

The far-field extrapolation is carried out in frequency domain [10] as the time-domain version is not very well suited for computing a whole hemisphere radiation patterns. Therefore, all field quantities in this section are considered as complex phasors, obtained by discrete Fourier transform of the time-domain data.

The spherical coordinate components of the far field electric intensity are

$$E_\theta = -j \frac{e^{-jkr}}{2\lambda r} (\eta N_\theta + L_\phi) \quad (20)$$

$$E_\phi = j \frac{e^{-jkr}}{2\lambda r} (-\eta N_\phi + L_\theta) \quad (21)$$

where λ is a wavelength, k the wavenumber, r is the distance of the observation point from the phase center and $\eta = \sqrt{\mu_0/\epsilon_0}$ is the free space wave impedance. Furthermore, the terms N_θ , N_ϕ and L_θ , L_ϕ are the spherical components of

$$\vec{N} = \int_A \vec{J}_s e^{jkr|_s \cos \psi} dA \quad (22)$$

$$\vec{L} = \int_A \vec{M}_s e^{jkr|_s \cos \psi} dA \quad (23)$$

These formulas represent the integration of surface electric and magnetic currents, \vec{J}_s and \vec{M}_s respectively, over the surface A , whereas $r|_s$ is the radius of the integration surface and ψ is the angle between radiusvectors of the far-field observation point and the integration element dA . The surface currents can be written in terms of electric and magnetic fields on the integration surface as

$$\vec{J}_s = \hat{r} \times \vec{H} = -H_\phi \hat{\theta} + H_\theta \hat{\phi} \quad (24)$$

$$\vec{M}_s = -\hat{r} \times \vec{E} = E_\phi \hat{\theta} - E_\theta \hat{\phi} \quad (25)$$

Here, $\hat{\theta}$ and $\hat{\phi}$ are local spherical coordinate unit vectors on the integration surface. Taking into account the far field unit vectors $\hat{\theta}'$, $\hat{\phi}'$ as well, we can decompose (22) and (23) into orthogonal components, $\vec{N} = N_\theta \hat{\theta}' + N_\phi \hat{\phi}'$, $\vec{L} = L_\theta \hat{\theta}' + L_\phi \hat{\phi}'$, and we obtain

$$\begin{aligned} E_\theta = & -j \frac{e^{-jkr}}{2\lambda r} \left[\sum_{j=1}^{J-1} \sum_{k=0}^{K-1} \left(E_\phi|_{s,j,k+0.5} \hat{\phi}' \hat{\theta}|_{j,k+0.5} \right. \right. \\ & \left. \left. + \eta H_\theta|_{s,j,k+0.5} \hat{\theta}' \hat{\phi}|_{j,k+0.5} \right) \right. \\ & \left. \times e^{jkr|_s \cos \psi|_{j,k+0.5}} \tilde{A}|_{s,j} \right. \\ & \left. - \sum_{j=0}^{J-1} \sum_{k=0}^{K-1} \left(E_\theta|_{s,j+0.5,k} \hat{\phi}' \hat{\phi}|_{j+0.5,k} \right. \right. \\ & \left. \left. + \eta H_\phi|_{s,j+0.5,k} \hat{\theta}' \hat{\theta}|_{j+0.5,k} \right) \right. \\ & \left. \times e^{jkr|_s \cos \psi|_{j+0.5,k}} A|_{s,j+0.5} \right] \quad (26) \\ E_\phi = & j \frac{e^{-jkr}}{2\lambda r} \left[\sum_{j=1}^{J-1} \sum_{k=0}^{K-1} \left(E_\phi|_{s,j,k+0.5} \hat{\theta}' \hat{\theta}|_{j,k+0.5} \right. \right. \end{aligned}$$

$$\begin{aligned} & \left. - \eta H_\theta|_{s,j,k+0.5} \hat{\phi}' \hat{\phi}|_{j,k+0.5} \right) \\ & \times e^{jkr|_s \cos \psi|_{j,k+0.5}} \tilde{A}|_{s,j} \\ & - \sum_{j=0}^{J-1} \sum_{k=0}^{K-1} \left(E_\theta|_{s,j+0.5,k} \hat{\theta}' \hat{\phi}|_{j+0.5,k} \right. \\ & \left. - \eta H_\phi|_{s,j+0.5,k} \hat{\phi}' \hat{\theta}|_{j+0.5,k} \right) \\ & \times e^{jkr|_s \cos \psi|_{j+0.5,k}} A|_{s,j+0.5} \end{aligned} \quad (27)$$

while approximating the integrals with summations. Concerning the surface area components, $\tilde{A}|_{s,j} = A_r|_{s,j}$ applies almost everywhere, except for $j = 1$ and $j = J - 1$. As the tangential field components of spherical FDTD are either not defined or set to zero on the poles, the surface areas related to the adjacent components have to be extended to compensate for this absence,

$$\tilde{A}_r|_{s,1} = \tilde{A}_r|_{s,J-1} = r^2|_s \Delta\phi \left(1 - \cos \frac{3\Delta\theta}{2} \right) \quad (28)$$

As the E and H field components in FDTD method are staggered in space, it is necessary to use some kind of averaging to obtain the desired quantity within the integration surface. The displacement of the field components in temporal dimension due to the leap-frog advance of FDTD does not have to be treated in any way, as the phase shift is negligible for small time steps implied by the lattice arrangement.

In the present algorithm, the integration surface is collocated with tangential electric components and magnetic fields have to be interpolated in radial direction. A geometric mean was chosen for this purpose, which brings significant improvement over commonly used linear interpolation [21].

V. ARRAY ELEMENT MODELING

When assembling the overall radiation pattern, the active element pattern approach [22] is used with advantage—only one element of the array is excited while the remaining are loaded with characteristic impedance of the feeder. It is evident, that in total 32 simulation runs are needed to achieve the freedom of virtually steering the beam by merely summing the particular radiation patterns weighted by excitation coefficients.

The array elements are monopoles with partial dielectric coating, as shown in Fig. 4a. They are actually the back sides of panel-type SMA connectors, mounted into sparings on the surface of the sphere. The metal sticks have radius $a = 0.65$ mm and length $l = 17.9$ mm, while the dielectric coatings with radius $b = 2.1$ mm reach only to $d = 15$ mm.

As the dimensions of the monopoles are apparently smaller than the largest FDTD cells, application of some kind of subcell FDTD technique is indicated. Such techniques for modeling of thin-wire antennas including treatment of the antenna tips were presented in [23] and [24]. In the present work, the thin-rod approximation of [16] was employed. To this end, axes of the monopoles were fitted into the primary FDTD grid, as required by [16]. However, from Fig. 4b,c it follows that although the spherical grid is coarse near the equator and, thus, the thin-rod approximation can be used without

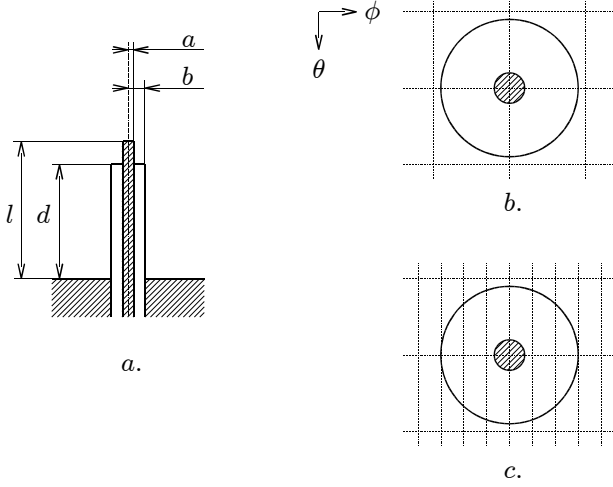


Fig. 4. Detail of the array element: a) dimensions of the coated monopole, b), c) top view of the corresponding mesh near the equator and near the poles.

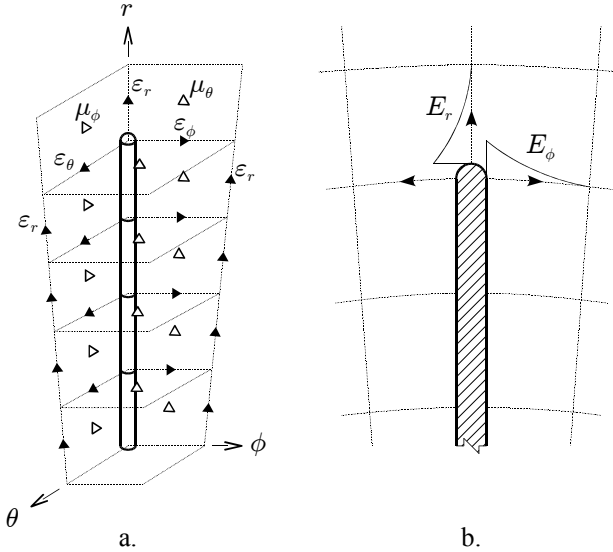


Fig. 5. Detail of the monopole rod: a) FDTD components adjacent to the rod, b) fields at the monopole tip.

complications, when approaching the poles the FDTD cells are thinner in the azimuth coordinate and some modifications are needed. Derivation of the particular modifications to [16] is demonstrated in Appendix, here only the resulting parameters used in the simulation are presented.

First modification is motivated by simplicity and efficiency: the integral factors L and S in [16] are merged and expressed in terms of material properties at the respective field positions (see Appendix and Fig. 5a). For instance, hyperbolic deformation of the radial electric fields adjacent to the monopole metal is respected in anisotropic relative permittivity elements

$$\varepsilon'_\theta = \frac{2l_\theta}{l_\phi} \left(\arctan \frac{l_\phi}{l_\theta} \right) \left(\ln \frac{l_\theta}{a} \right)^{-1} \quad (29)$$

$$\varepsilon'_\phi = \frac{2l_\phi}{l_\theta} \left(\arctan \frac{l_\theta}{l_\phi} \right) \left(\ln \frac{l_\phi}{a} \right)^{-1} \quad (30)$$

with l_θ and l_ϕ as the lengths of the local grid segments. If the permittivity elements are computed also in the positions of circulating magnetic fields, then the relative permeability elements are simply

$$\mu'_\theta = (\varepsilon'_\phi)^{-1} \quad (31)$$

$$\mu'_\phi = (\varepsilon'_\theta)^{-1} \quad (32)$$

The primes express the fact that ε' and μ' are only coefficients to the permittivity and permeability values (13) and (14), respectively.

When the grid segment is completely embedded in the dielectric coating, the quantities (29) and (30) are just multiplied by the dielectric constant of the coating $\varepsilon'_{\text{diel}} = 2.1$ (Teflon).

Grid segments that are not adjacent to the metallic rod may, however, lie completely or partially in the dielectric coating. In such cases, average dielectric constants ε'_r , ε'_θ and ε'_ϕ are defined simply

$$\varepsilon' = \frac{l_1 + l_2}{l_1(\varepsilon'_1)^{-1} + l_2(\varepsilon'_2)^{-1}} \quad (33)$$

where ε'_1 and ε'_2 are the material constants spanning l_1 and l_2 portions, respectively, of the total cell edge length $l_1 + l_2$.

If the adjacent primary grid segments normal to the metallic rod intersect both metal-dielectric and dielectric-air interfaces, modifications are made to the ε'_θ and ε'_ϕ constants

$$\varepsilon'_\theta = \frac{2l_\theta}{l_\phi} \left(\arctan \frac{l_\phi}{l_\theta} \right) \left[(\varepsilon'_{\text{diel}})^{-1} \ln \frac{b}{a} + \ln \frac{l_\theta}{b} \right]^{-1} \quad (34)$$

$$\varepsilon'_\phi = \frac{2l_\phi}{l_\theta} \left(\arctan \frac{l_\theta}{l_\phi} \right) \left[(\varepsilon'_{\text{diel}})^{-1} \ln \frac{b}{a} + \ln \frac{l_\phi}{b} \right]^{-1} \quad (35)$$

originating from the integrals in [16].

Cylindrical monopole ends are substituted by hemispheres as suggested in [16], to appropriately model the end effects. Nevertheless, the position of the hemispherical tip is different from [16]—the center of the sphere is placed in the intersection of the primary grid lines (see Fig. 5b). This allows us to assign the $1/r^2$ behavior not only to the collinear E -field, but to all radial E -fields emerging from the monopole tip, yielding equivalent material properties

$$\varepsilon'_r = \frac{4l_r}{l_\theta l_\phi} (a^{-1} - l_r^{-1})^{-1} \arctan \frac{l_\theta l_\phi}{l_r \sqrt{l_r^2 + l_\theta^2 + l_\phi^2}} \quad (36)$$

$$\varepsilon'_\theta = \frac{4l_\theta}{l_r l_\phi} (a^{-1} - l_\theta^{-1})^{-1} \arctan \frac{l_r l_\phi}{l_\theta \sqrt{l_r^2 + l_\theta^2 + l_\phi^2}} \quad (37)$$

$$\varepsilon'_\phi = \frac{4l_\phi}{l_r l_\theta} (a^{-1} - l_\phi^{-1})^{-1} \arctan \frac{l_r l_\theta}{l_\phi \sqrt{l_r^2 + l_\theta^2 + l_\phi^2}} \quad (38)$$

Because the dielectric coating of the monopole does not reach the tip, the dielectric constant is not used here.

The rest of the rules governing the material constants follow the stability of the FDTD algorithm, in the sense of similar rules presented in [16] (see also Appendix). First, the

tangential H -fields around the tip (with radial coordinates i_{tip}) are updated using magnetic constants

$$\mu'_{\theta}|_{i_{\text{tip}}-0.5} = \max \left\{ \mu'_{\theta}|_{i_{\text{tip}}-0.5}; (\varepsilon'_{\phi}|_{i_{\text{tip}}-1})^{-1}; (\varepsilon'_{\phi}|_{i_{\text{tip}}})^{-1} \right\} \quad (39)$$

$$\mu'_{\phi}|_{i_{\text{tip}}-0.5} = \max \left\{ \mu'_{\phi}|_{i_{\text{tip}}-0.5}; (\varepsilon'_{\theta}|_{i_{\text{tip}}-1})^{-1}; (\varepsilon'_{\theta}|_{i_{\text{tip}}})^{-1} \right\} \quad (40)$$

$$\mu'_{\theta}|_{i_{\text{tip}}+0.5} = \max \left\{ 1; (\varepsilon'_{\phi}|_{i_{\text{tip}}})^{-1}; (\varepsilon'_{\phi}|_{i_{\text{tip}}+0.5})^{-1} \right\} \quad (41)$$

$$\mu'_{\phi}|_{i_{\text{tip}}+0.5} = \max \left\{ 1; (\varepsilon'_{\theta}|_{i_{\text{tip}}})^{-1}; (\varepsilon'_{\theta}|_{i_{\text{tip}}+0.5})^{-1} \right\} \quad (42)$$

dependent on neighboring modified dielectric constants.

Similarly, the neighboring magnetic fields parallel to the monopole have to be stabilized using

$$\mu'_r = \max \left\{ 1; (\varepsilon'_{\theta})^{-1}; (\varepsilon'_{\phi})^{-1} \right\} \quad (43)$$

Finally, the parallel electric fields adjacent to the modified μ'_{θ} and μ'_{ϕ} positions need to be scaled in case the modifications of the respective magnetic constants result in too low values

$$\varepsilon'_r = \max \left\{ \varepsilon'_r; (2\mu'_{\theta})^{-1} \right\} \quad (44)$$

$$\varepsilon'_r = \max \left\{ \varepsilon'_r; (2\mu'_{\phi})^{-1} \right\} \quad (45)$$

The electric field components E_r correlated with the metallic rod are zeroed along the monopole, simulating a perfect electric conductor. The first segment of the monopole, centered at $0.5, j, k$, serves as a lumped load substituting for a coaxial feeder. Electric current flowing through the load is computed using the integral representation of fields (see also Appendix)

$$\begin{aligned} I|_{0.5,j,k} = & \left(H_{\theta}|_{0.5,j,k-0.5} - H_{\theta}|_{0.5,j,k+0.5} \right) l_{\theta}|_{0.5} \\ & + H_{\phi}|_{0.5,j+0.5,k} l_{\phi}|_{0.5,j+0.5} \\ & - H_{\phi}|_{0.5,j-0.5,k} l_{\phi}|_{0.5,j-0.5} \end{aligned} \quad (46)$$

Total voltage across the filament V is formed by voltage of the load with resistance R_s and, eventually, a source voltage V_s (when the particular monopole is exciting the antenna)

$$V = IR_s + V_s \quad (47)$$

Conversion to the corresponding electric field is then straightforward

$$E_r|_{0.5,j,k} = \frac{V}{l_r} \quad (48)$$

Input impedance of the monopole is $Z_{11} = -V_1/I_1$, and the s-parameters are expressed

$$s_{11} = \frac{Z_{11} - R_s}{Z_{11} + R_s} \quad (49)$$

$$s_{21} = \frac{-2I_2/I_1}{Z_{11}/R_s + 1} \quad (50)$$

where the index 1 denotes number of the exciting monopole and index 2 can be arbitrary monopole selected for output observations.

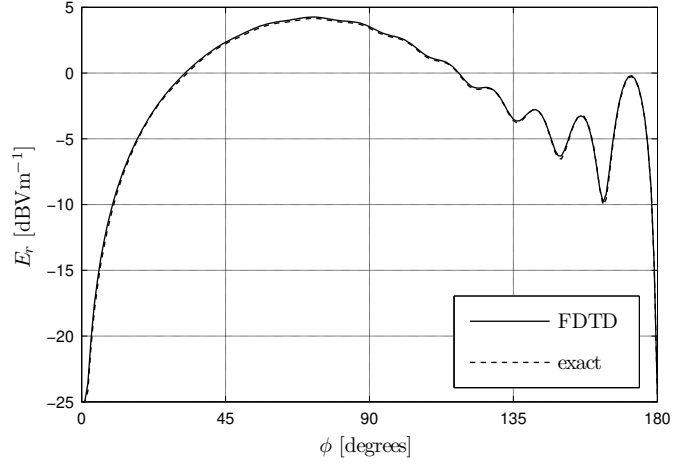


Fig. 6. Magnitude of radial electric field E_r positioned $0.5\Delta r$ over the sphere surface, for FDTD and exact solutions, $f = 5.9$ GHz.

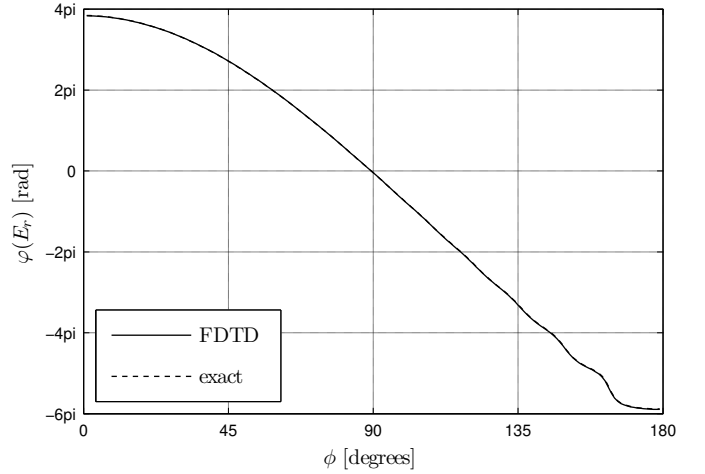


Fig. 7. Phase of radial electric field E_r positioned $0.5\Delta r$ over the sphere surface, for FDTD and exact solutions, $f = 5.9$ GHz.

VI. NUMERICAL RESULTS

The FDTD simulation used $2^\circ \times 2^\circ$ resolution in the θ and ϕ directions, making the θ -oriented cell edges span from 3.4 mm for the sphere surface to 5.6 mm on the termination of the PML (see Eq. 8), while the ϕ -oriented edges start from as low as 0.06 mm at the sphere poles (9). The length of the cell filament in the radial direction was $l_r = 4.3125$ mm, tailored to fit four times into the length of the monopole respecting the radius of the cap (see Fig. 5a). Given the minimum edge lengths, the time-step was approximately determined by

$$\Delta t \leq \frac{1}{c\sqrt{l_r^{-2} + l_\theta^{-2} + l_\phi^{-2}}} \quad (51)$$

where c represents the speed of light. This yielded $\Delta t \doteq 0.2$ ps, which was experimentally proven as stable.

The main computational domain was 7-cell thick in radial direction, followed by the anisotropic PML layer with depth of 5 cells. The excitation pulse was Gaussian weighted sinusoid with center frequency 4.5 GHz and characteristic decay $\tau = 156$ ps. The overall number of time-steps was chosen 20000,

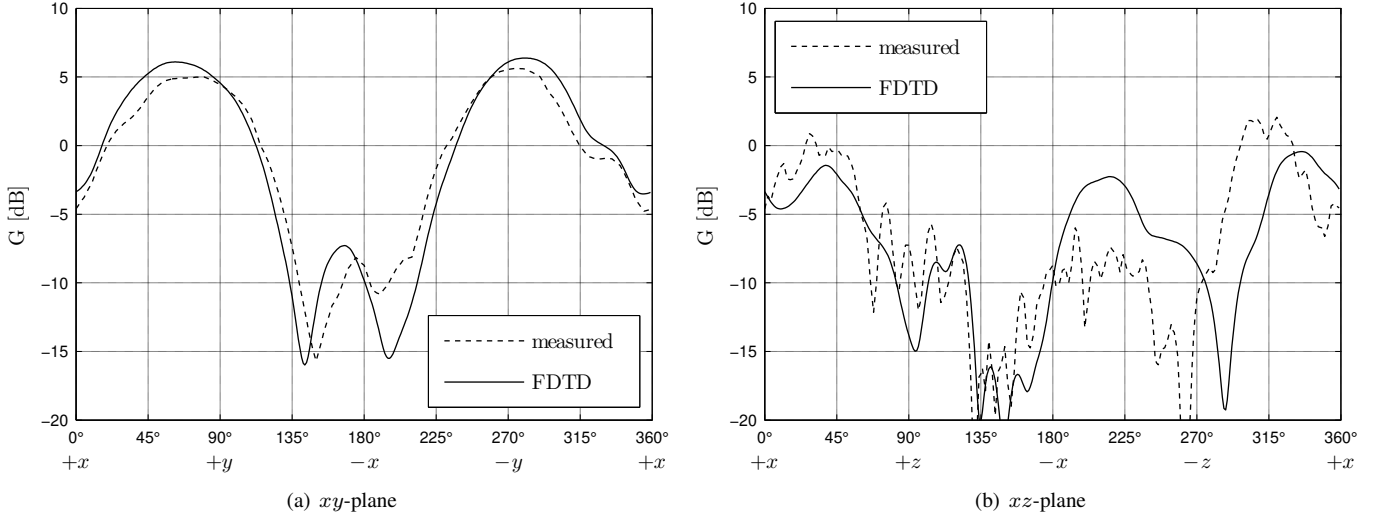


Fig. 8. Comparison of FDTD and measured mixed polarization gain of the spherical antenna with monopole no. 2 ($\phi = 352^\circ$, $\theta = 154^\circ$) excited, at frequency 5.9 GHz

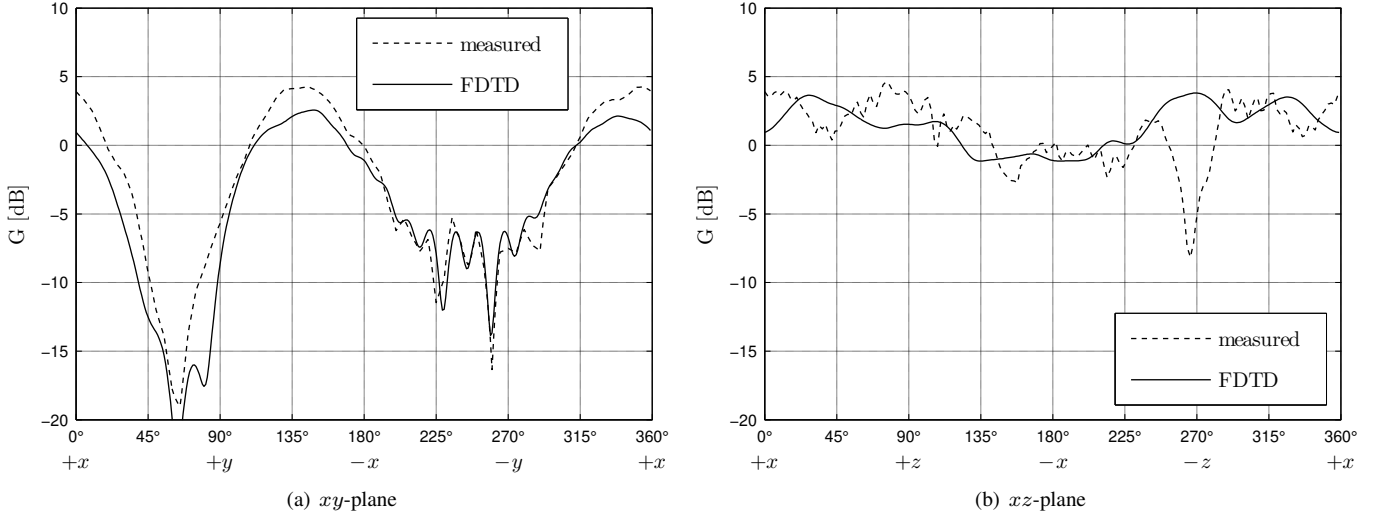


Fig. 9. Comparison of FDTD and measured mixed polarization gain of the spherical antenna with monopole no. 17 ($\phi = 64^\circ$, $\theta = 96^\circ$) excited, at frequency 5.9 GHz

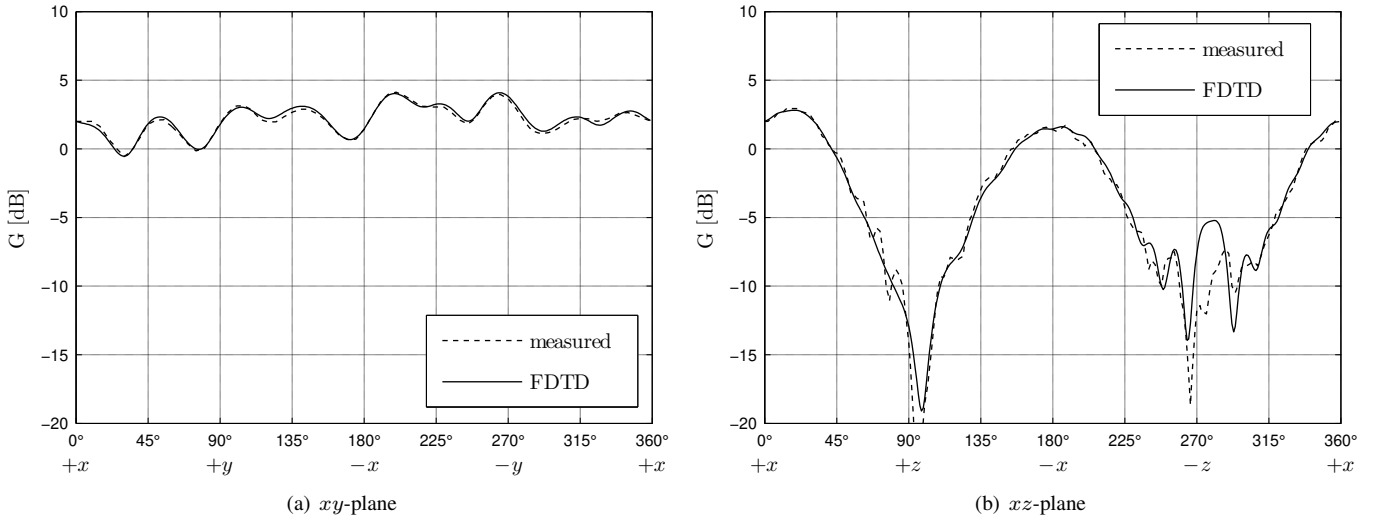


Fig. 10. Comparison of FDTD and measured mixed polarization gain of the spherical antenna with monopole no. 32 ($\phi = 224^\circ$, $\theta = 12^\circ$) excited, at frequency 5.9 GHz

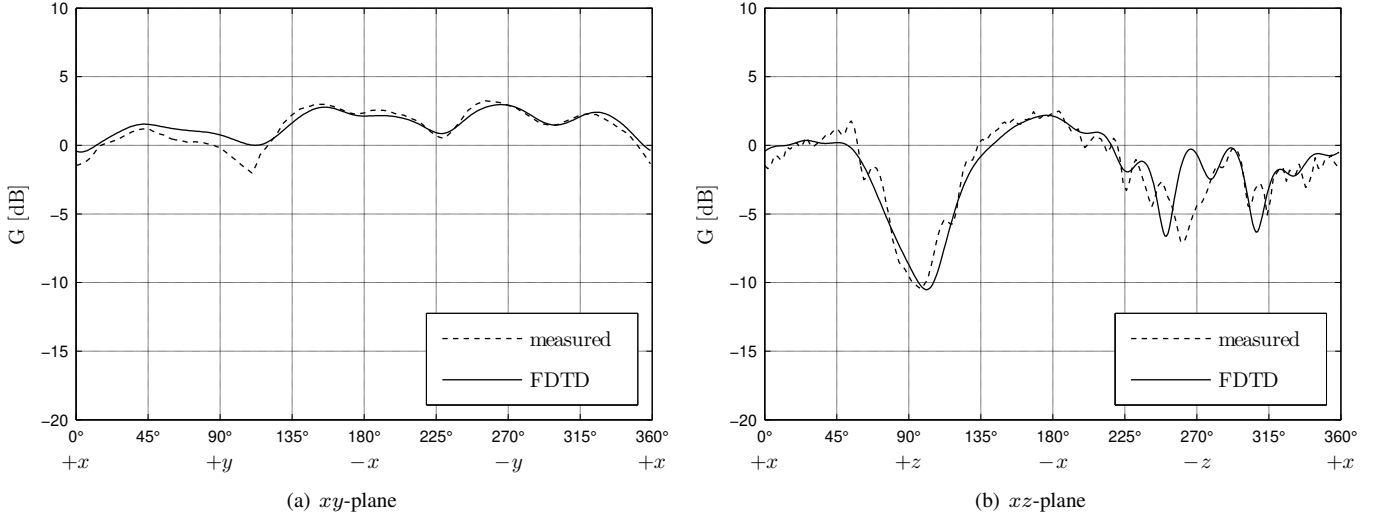


Fig. 11. Comparison of FDTD and measured mixed polarization gain of the spherical antenna with monopole no. 32 ($\phi = 224^\circ$, $\theta = 12^\circ$) excited, at frequency 3.0 GHz

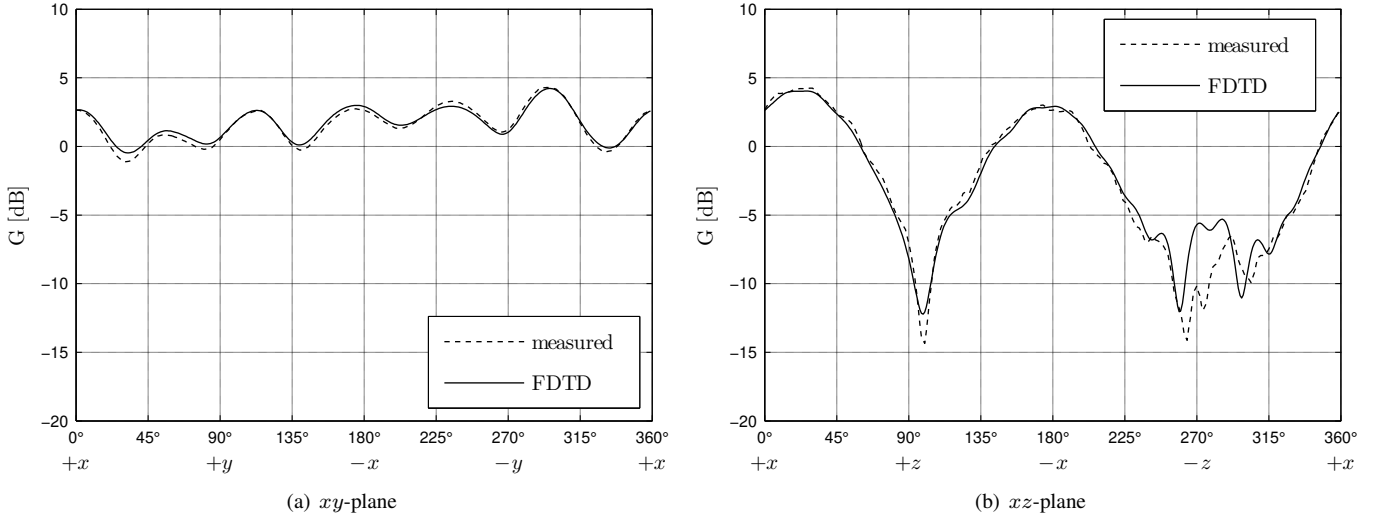


Fig. 12. Comparison of FDTD and measured mixed polarization gain of the spherical antenna with monopole no. 32 ($\phi = 224^\circ$, $\theta = 12^\circ$) excited, at frequency 4.5 GHz

as beyond this point the energy in the grid dropped below 10^{-8} of its peak value.

Correctness of the described numerical algorithm was first validated by running a simulation of bare sphere (without monopoles) and comparing it with known analytical solution. One radial electric field component adjacent to the sphere surface was excited as transparent (soft) current source and far-field pattern was rendered. Such a case is reciprocal to observing radial electric field on a sphere illuminated by a plane wave, where the exact solution is available [25].

Let us assume that the plane wave of magnitude 1 Vm^{-1} is impinging on the sphere from direction given by $\theta = \pi/2$, $\phi = 0$. The magnitude and the phase of the E_r component half a cell above the surface of the sphere is shown in Fig. 6 and 7, respectively. Maximum difference of the exact and FDTD computed data is less than 0.6 dB in magnitude and 5 degrees in phase, both occurring only in the minima of the

field.

Figs. 8–14 show the radiation patterns with all the monopoles present. Only one monopole is excited in each case and the mixed polarization gain, i. e. the gain of the antenna composed of both polarization waves, is observed. The patterns were plotted for three monopoles representing typical positions on the sphere: close to the mounting rod, near the equator and near the top of the sphere (monopole numbers 2, 17 and 32, respectively—for reference, see Fig. 1). In Figs. 8–12, only cross sections of the full hemisphere radiation patterns are presented, namely in the xy and xz planes. The particular directions of the axes are emphasized on the horizontal scales. As a supplement, two examples of the full hemisphere pattern in color scale are given in Figs. 13 and 14.

It can be seen from the figures that the discrepancies between the FDTD and measured results are more pronounced in vertical directions (i.e. $+z$ and $-z$ axes) and generally with

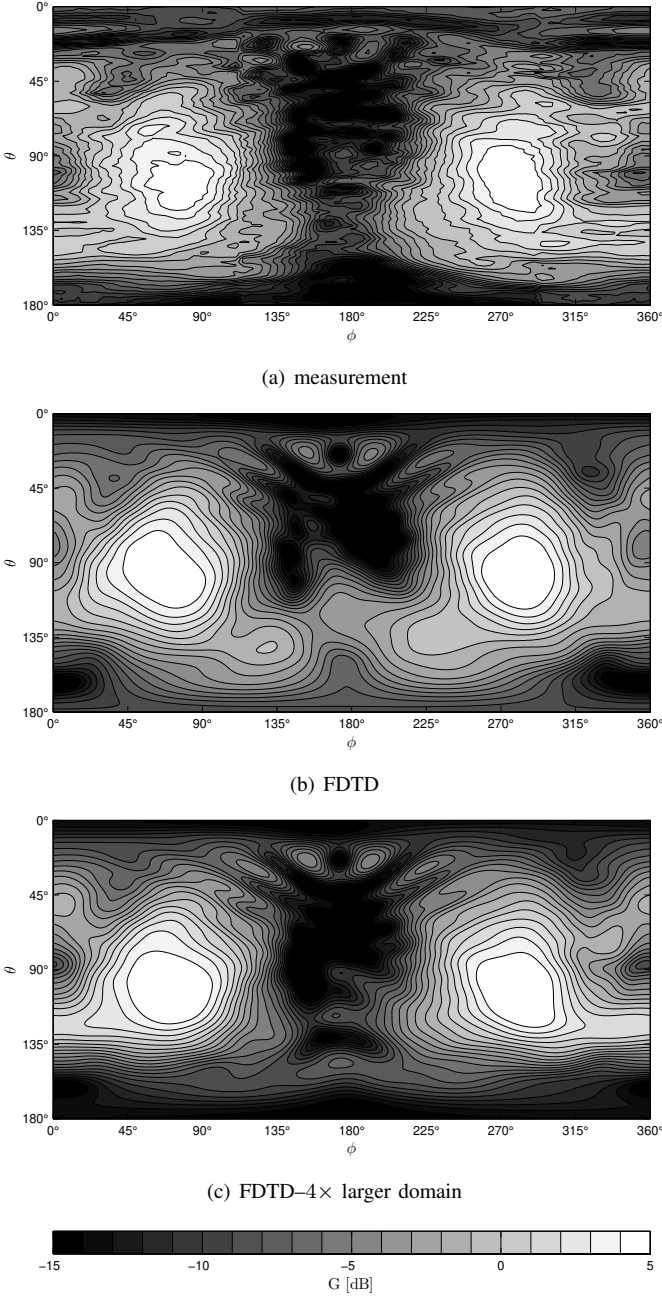


Fig. 13. Comparison of FDTD and measured mixed polarization gain in full hemisphere of the spherical antenna with monopole no. 2 ($\phi = 352^\circ$, $\theta = 154^\circ$) excited, at frequency 5.9 GHz.

monopoles closer to the mounting rod. There is a strong belief that these effects are due to finite length of the rod assumed in simulations, while the measurements were carried out with long rod positioned on relatively massive metallic mount (see Fig. 19). This reasoning is supported by Fig. 13(c), where the radiation pattern of the monopole no. 2 is obtained from simulation with four times larger computational domain in radial direction (28 cells instead of 7), thus including four times longer portion of the mounting rod. However, in global sense the FDTD-obtained patterns are in good agreement with the measurement results, as can be seen from the full hemisphere diagrams in Figs. 13 and 14.

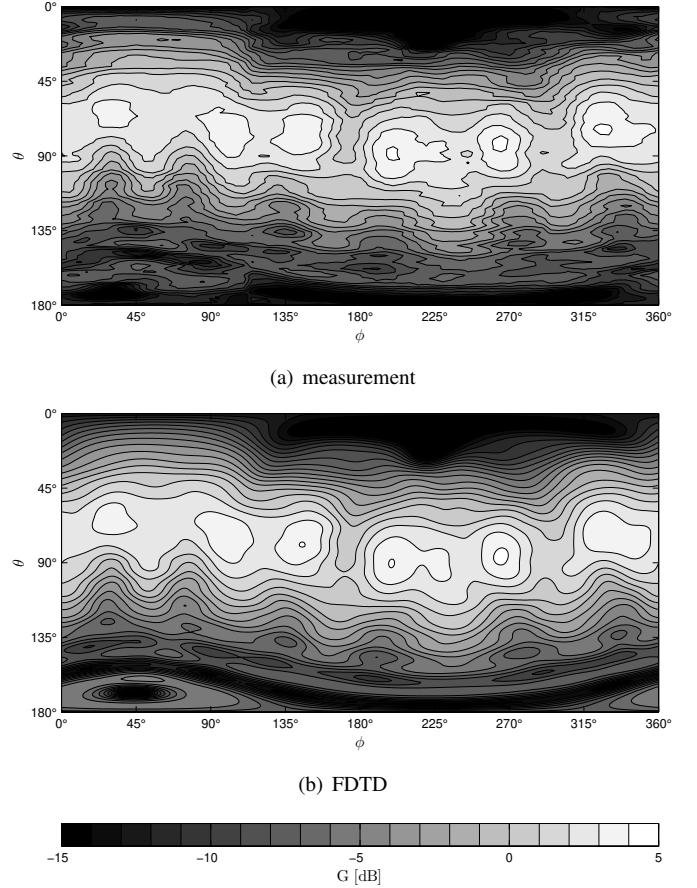


Fig. 14. Comparison of FDTD and measured mixed polarization gain in full hemisphere of the spherical antenna with monopole no. 32 ($\phi = 224^\circ$, $\theta = 12^\circ$) excited, at frequency 5.9 GHz.

Next, the matching and coupling of the monopoles are analysed. In Figs. 15–17, the s -parameters are evaluated for various pairs of monopoles, again covering positions near the mounting rod (bottom part), the equator and the top of the sphere, and close and distant couplings (for reference of the monopole numbers, see Fig. 1). The FDTD simulation data is obtained by means of discrete Fourier transform of recorded time responses.

Again, the most visible differences occur with monopoles closer to the rod and, of course, with long distance coupling, as the influence of the surroundings is stronger here. However, the errors occur below -20 dB and do not contribute significantly to the overall results. On the other hand, the matching coefficients are accurate for all three tested monopoles.

Finally, Fig. 18 shows the same s -parameters as in Fig. 17, that is matching of the monopole no. 32 and its coupling with monopole no. 31, but without the thin-rod approximation described in Section V. Here, the monopoles are modeled by merely zeroing four collinear filaments of radial electric field stemming from the sphere. The absence of the dielectrics and ignoring the singular effects causes the resonance of the monopole to be slightly shifted, as can be seen from Fig. 18.

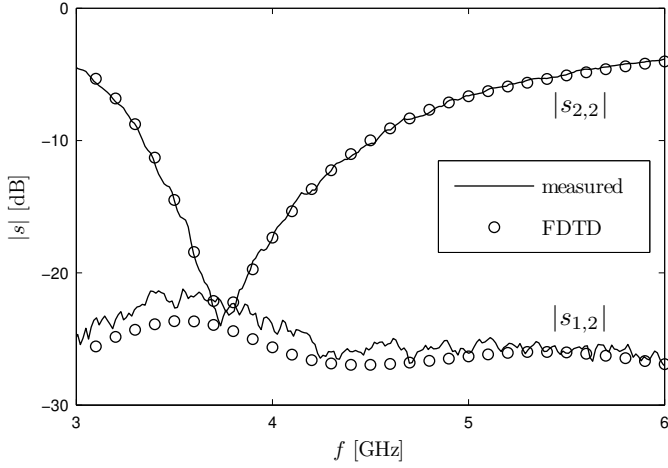


Fig. 15. Magnitude of s -parameters between monopoles no. 1 ($\phi = 80^\circ$, $\theta = 152^\circ$) and no. 2 ($\phi = 352^\circ$, $\theta = 154^\circ$): comparison of measured and FDTD results

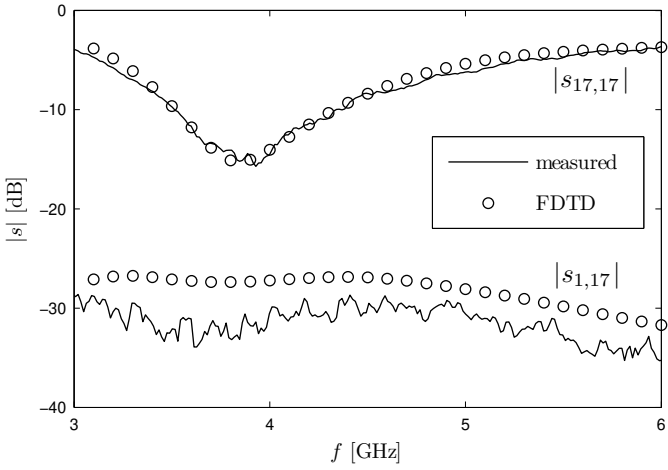


Fig. 16. Magnitude of s -parameters between monopoles no. 1 ($\phi = 80^\circ$, $\theta = 152^\circ$) and no. 17 ($\phi = 64^\circ$, $\theta = 96^\circ$): comparison of measured and FDTD results

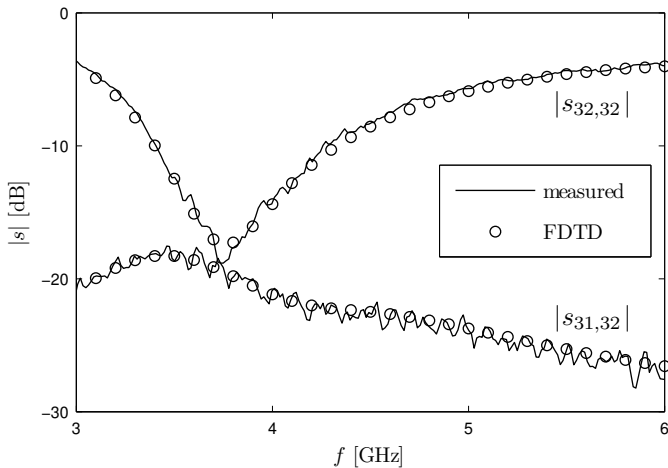


Fig. 17. Magnitude of s -parameters between monopoles no. 31 ($\phi = 60^\circ$, $\theta = 26^\circ$) and no. 32 ($\phi = 224^\circ$, $\theta = 12^\circ$): comparison of measured and FDTD results

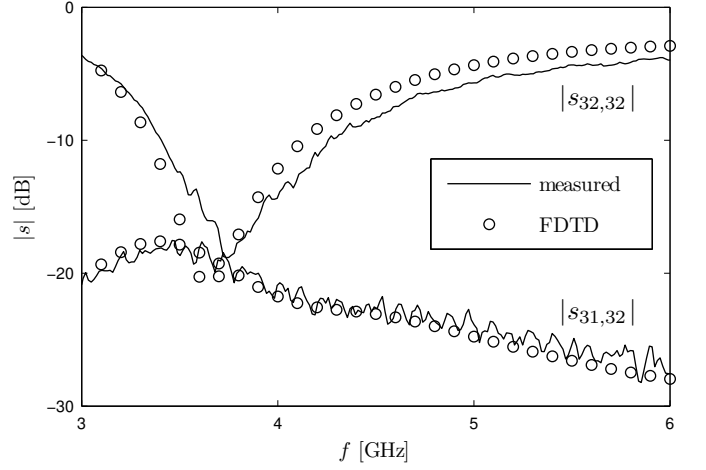


Fig. 18. Magnitude of s -parameters between monopoles no. 31 ($\phi = 60^\circ$, $\theta = 26^\circ$) and no. 32 ($\phi = 224^\circ$, $\theta = 12^\circ$): comparison of measured and FDTD results without thin-rod approximations

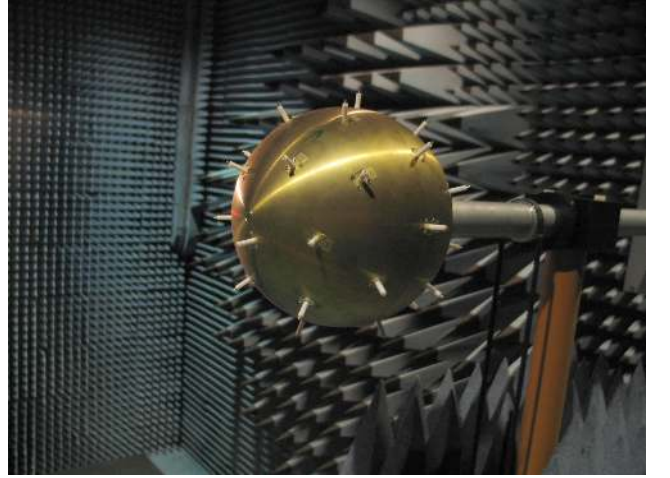


Fig. 19. The spherical array antenna with the metallic rod during the measurement in anechoic chamber.

VII. CONCLUSION

The numerical analysis of spherical array of monopoles using spherical-coordinate FDTD method was presented. The simplified problem of bare sphere illumination showed an excellent agreement with known exact solution, which anticipated the ability of the chosen method to provide accurate results. This was finally proven in confrontation with data obtained from measurement. The authors believe that the presented description of the approach will be helpful to others in applying the method either to spherical phased arrays or to different problems of similar geometry.

APPENDIX

Some definitions presented in Section V originating from the thin-rod approximation technique [16] are clarified below.

Let us assume that the Cartesian coordinate system used in [16] is associated with the monopole so that $x \rightarrow \theta$, $y \rightarrow \phi$

and $z \rightarrow r$. Then Eq. 10 from [16] can be written

$$L_{E_\theta} = 0.5 l_\theta \ln \frac{l_\theta}{a} \quad (52)$$

and Eq. 16 in [16] is

$$S_{E_{\phi r}} = l_r l_\theta \arctan \frac{l_\phi}{l_\theta} \quad (53)$$

where the grid segments are $\Delta x \rightarrow l_\theta$, $\Delta y \rightarrow l_\phi$ and $\Delta z \rightarrow l_r$.

According to [16], the length coefficients L_{E_θ} should be used instead of particular l_θ in (4) and (6). Similarly, $S_{E_{\phi r}}$ substitutes for cell face area A_θ in (2). To preserve the simplicity and efficiency of the FDTD algorithm in the present work, the field values in the vicinity of the monopole are understood as *average* values along the cell edges. This allows us to use the original integral formulation of the spherical FDTD (1)–(6) without disturbances, whereas the information about the nonstandard fields near the monopoles is hidden in the ε and μ coefficients.

For instance, the θ -oriented electric field integrated over the corresponding segment is

$$E_\theta^{(\text{average})} l_\theta = E_\theta^{(\text{pointwise})} L_{E_\theta} \quad (54)$$

This means that (4) and (6) do not need to be modified, while the update equation (2) is now

$$\begin{aligned} E_\theta|_{i,j+0.5,k}^{n+1} &= E_\theta|_{i,j+0.5,k}^n + \frac{L_{E_\theta} \Delta t A_\theta|_{i,j+0.5}}{l_\theta | \varepsilon_\theta|_{i,j+0.5,k} S_{E_{\phi r}} A_\theta|_{i,j+0.5}} \\ &\times \left[\left(H_r|_{i,j+0.5,k+0.5}^{n+0.5} - H_r|_{i,j+0.5,k-0.5}^{n+0.5} \right) l_r \right. \\ &\quad - H_\phi|_{i+0.5,j+0.5,k}^{n+0.5} l_\phi|_{i+0.5,j+0.5} \\ &\quad \left. + H_\phi|_{i-0.5,j+0.5,k}^{n+0.5} l_\phi|_{i-0.5,j+0.5} \right] \quad (55) \end{aligned}$$

The original form of (2) is restored by grouping the extra terms into additional dielectric coefficient

$$\varepsilon'_\theta = \frac{l_\theta | \varepsilon_\theta|_{i,j+0.5}}{L_{E_\theta} A_\theta|_{i,j+0.5}} \quad (56)$$

Since the surface area A_θ can be expressed as $l_r l_\phi$ (compare (7) and (9) with (11)), we obtain (29). The expression (30) is derived analogically.

By comparing Eqs. 10 and 16 with Eqs. 11 and 17 in [16] we see that the additional permeability coefficients μ' can be computed similarly and, what is more, the resulting formulas are reciprocal to ε'_θ and ε'_ϕ , hence (31) and (32) apply.

In case that the primary grid segment is intersected by the dielectric boundary, the effective dielectric constant ε_{eff} of the corresponding E-field is computed from Eq. 32 in [16]

$$\varepsilon_{\text{eff}} = \ln \frac{l_\theta}{a} \left[\varepsilon_{\text{diel}}^{-1} \ln \frac{b}{a} + \ln \frac{l_\theta}{b} \right]^{-1} \quad (57)$$

where the background is considered vacuum. Multiplying (29) with (57) we obtain the resulting (34) and, analogically, substituting l_θ with l_ϕ in (57), we obtain (35) from (30).

The same procedure as for expressing ε'_θ above can be applied to get the auxiliary coefficients at the monopole tip. Formula (36) for the vertical segment is constructed using Eq. 22 in [16]

$$L_{E_r} = (0.5 l_r)^2 [a^{-1} - l_r^{-1}] \quad (58)$$

and Eq. 26 in [16]

$$S_{E_{\theta\phi}} = l_r^2 \arctan \frac{l_\theta l_\phi}{l_r(l_r^2 + l_\theta^2 + l_\phi^2)^{1/2}} \quad (59)$$

where the different position of the tip is respected by assigning $(0.5\Delta z + a) \rightarrow 0.5l_r$, $(\Delta z + a) \rightarrow l_r$ and, of course, $\delta_x \rightarrow l_\theta/2$, $\delta_y \rightarrow l_\phi/2$, $\delta_z \rightarrow l_r/2$. Formulas (37) and (38) are derived by just permuting the edge lengths.

The stability criteria introduced in (39)–(45) follow the assumption that a product of any neighboring dielectric constants must be higher or equal to 1 in order to avoid superluminal propagation in the grid leading to instability. We take the μ'_θ coefficient in (39) as an example. First, we scale the neighboring E_ϕ components by ε'_ϕ

$$E'_\phi = \varepsilon'_\phi E_\phi \quad (60)$$

so that the equation (3) is void of any correction and need not be treated anymore. Now, (5) at the point $(i_{\text{tip}} - 0.5, j, k + 0.5)$ can be written as

$$\begin{aligned} H_\theta|_{i_{\text{tip}}-0.5,j,k+0.5}^{n+0.5} &= H_\theta|_{i_{\text{tip}}-0.5,j,k+0.5}^{n-0.5} - \frac{\Delta t / A_\theta|_{i_{\text{tip}}-0.5,j}}{\mu_\theta|_{i_{\text{tip}}-0.5,j,k+0.5}} \\ &\times \left[\left(E_r|_{i_{\text{tip}}-0.5,j,k+1}^n - E_r|_{i_{\text{tip}}-0.5,j,k}^n \right) l_r (\mu'_\theta)^{-1} \right. \\ &\quad - E_\phi|_{i_{\text{tip}},j,k+0.5}^n l_\phi|_{i_{\text{tip}},j} (\mu'_\theta \varepsilon'_\phi|_{i_{\text{tip}}})^{-1} \\ &\quad \left. + E_\phi|_{i_{\text{tip}}-1,j,k+0.5}^n l_\phi|_{i_{\text{tip}}-1,j} (\mu'_\theta \varepsilon'_\phi|_{i_{\text{tip}}-1})^{-1} \right] \quad (61) \end{aligned}$$

Stability is enforced by setting $\mu'_\theta \varepsilon'_\phi|_{i_{\text{tip}}} \geq 1$, $\mu'_\theta \varepsilon'_\phi|_{i_{\text{tip}}-1} \geq 1$, i. e. μ'_θ is not allowed to be lower than the reciprocal values of neighboring ε'_ϕ coefficients. At the same time, however, the new value of μ'_θ should not be lower than the original μ'_θ , hence equation (39) applies. Similar rule can be derived for (40). In (41)–(43), the underlying coefficient has not been introduced before, therefore its value is 1. Finally, in (44), (45) the neighboring μ' coefficients can drop to 0.5 without sacrificing stability, which is due to the presence of metal on one side of the cell.

It is worth noting that the feed current in (46) is also expressed in terms of understanding the field values as averages over the line segments, which substantially simplifies the formulation. If for some reason one needs to know the pointwise field values, they can be easily extracted in terms of (54).

ACKNOWLEDGMENT

One of the authors (JBA) thanks DoCoMo Euro-Labs for economic support. The authors would also like to thank Dr. Tim Brown for his comments on the manuscript.

REFERENCES

- [1] M. Hoffman, "Conventions for the analysis of spherical arrays," *IEEE Trans. Antennas Propagat.*, vol. 11, no. 4, pp. 390–393, July 1963.
- [2] D. L. Sengupta, T. M. Smith, and R. W. Larson, "Radiation characteristics of a spherical array of circularly polarized elements," *IEEE Trans. Antennas Propagat.*, vol. 16, no. 1, pp. 2–7, Jan. 1968.
- [3] R. H. MacPhie, "The element density of a spherical antenna array," *IEEE Trans. Antennas Propagat.*, vol. 16, no. 1, pp. 125–127, Jan. 1968.

- [4] H. E. Schrank, "Basic theoretical aspects of spherical phased arrays," in *Phased Array Antennas, Proc. 1970 Phased Array Antenna Symp.*, A. A. Oliner and G. H. Knittel, Eds., Polytechnic Institute of Brooklyn, Farmingdale, NY: Artech House, 1972, pp. 323–327.
- [5] R. J. Stockton and R. P. Hockensmith, "Application of spherical arrays—a simple approach," in *Antennas and Propagation Society International Symposium, 1977*, vol. 15, June 1977, pp. 202–205.
- [6] S. Horiguchi, T. Ishizone, and Y. Mushiaki, "Radiation characteristics of spherical triangular array antenna," *IEEE Trans. Antennas Propagat.*, vol. 33, no. 4, pp. 472–476, Apr. 1985.
- [7] K. Kalliola, H. Laitinen, L. I. Vaskelainen, and P. Vainikainen, "Real-time 3-D spatial-temporal dual-polarized measurement of wideband radio channel at mobile station," *IEEE Trans. Instrum. Meas.*, vol. 49, no. 2, pp. 439–448, Apr. 2000.
- [8] A. Vallecchi and G. Biffi Gentili, "Broad band full scan coverage dual polarised spherical conformal phased array," *J. of Electromagn. Waves and Appl.*, vol. 16, no. 3, pp. 385–401, 2002.
- [9] J. Verhaevert, E. Van Lil, and A. Van de Capelle, "Three-dimensional monopole antenna for direction of arrival determination," vol. 151, no. 2, Apr. 2004, pp. 121–126.
- [10] A. Taflov and S. C. Hagness, *Computational Electrodynamics: The Finite-Difference Time-Domain Method*, 2nd ed. Norwood, MA: Artech House, 2000.
- [11] K. Du, N. Farahat, H. A. Raouf, T. Su, W. H. Yu, and R. Mittra, "Simulation of circular patch antenna on a sphere using the conformal finite difference time domain (CFDTD) algorithm," in *Antennas and Propagation Society International Symposium, 2003*, vol. 2, June 2003, pp. 988–991.
- [12] R. Holland, "THREDS: A finite-difference time-domain EMP code in 3D spherical coordinates," *IEEE Trans. Nucl. Sci.*, vol. 30, no. 6, pp. 4592–4595, Dec. 1983.
- [13] G. Liu and C. A. Grimes, "Spherical-coordinate FDTD analysis of conical antennas mounted above finite ground planes," *Microw. Opt. Techn. Lett.*, vol. 23, no. 2, pp. 78–82, Oct. 1999.
- [14] C. Phongcharoenpanich, E. Khoomwong, and M. Krairiksh, "Simulations of EM fields inside the concentric conducting spherical cavity using the FD-TD in spherical coordinates," in *Proc. 5th International Symposium on Antennas, Propagation and EM Theory (ISAPE 2000)*, Aug. 2000, pp. 142–145.
- [15] J. J. Simpson and A. Taflov, "Three-dimensional FDTD modeling of impulsive ELF propagation about the Earth-sphere," *IEEE Trans. Antennas Propagat.*, vol. 52, no. 2, pp. 443–451, Feb. 2004.
- [16] J. Nadobny, R. Pontalti, D. Sullivan, W. Włodarczyk, A. Vaccari, P. Deuffhard, and P. Wust, "A thin-rod approximation for the improved modeling of bare and insulated cylindrical antennas using the FDTD method," *IEEE Transactions on Antennas and Propagation*, vol. 51, no. 8, pp. 1780–1796, Aug. 2003.
- [17] K. S. Yee, "Numerical solution of initial boundary value problems involving Maxwell's equations in isotropic media," *IEEE Trans. Antennas Propagat.*, vol. 14, no. 3, pp. 302–307, May 1966.
- [18] J. S. Juntunen and T. D. Tsiboukis, "Reduction of numerical dispersion in FDTD method through artificial anisotropy," *IEEE Trans. Microwave Theory Tech.*, vol. 48, no. 4, pp. 582–588, Apr. 2000.
- [19] F. L. Teixeira and W. C. Chew, "Systematic derivation of anisotropic PML absorbing media in cylindrical and spherical coordinates," *IEEE Microwave Guided Wave Lett.*, vol. 7, no. 11, pp. 371–373, Nov. 1997.
- [20] S. D. Gedney, "An anisotropic perfectly matched layer-absorbing medium for the truncation of FDTD lattices," *IEEE Trans. Antennas Propagat.*, vol. 44, no. 12, pp. 1630–1639, Dec. 1996.
- [21] J. Fang and D. Xeu, "Numerical errors in the computation of impedances by FDTD method and ways to eliminate them," *IEEE Microwave Guided Wave Lett.*, vol. 5, no. 1, pp. 6–8, Jan. 1995.
- [22] D. M. Pozar, "The active element pattern," *IEEE Trans. Antennas Propagat.*, vol. 42, no. 8, pp. 1176–1178, Aug. 1994.
- [23] M. Douglas, M. Okoniewski, and M. A. Stuchly, "Accurate modeling of thin-wire antennas in the FDTD method," *Microw. Opt. Techn. Lett.*, vol. 21, no. 4, pp. 261–265, 1999.
- [24] R. Mäkinen, J. S. Juntunen, and M. A. Kivikoski, "An improved thin-wire model for FDTD," *IEEE Trans. Microwave Theory Tech.*, vol. 50, no. 5, pp. 1245–1255, May 2002.
- [25] J. A. Stratton, *Electromagnetic Theory*. New York: McGraw-Hill, 1941.



Ondřej Franek was born in 1977. He received his master's degree (Ing., with honors) in electronics and communication with minor biomedical engineering certificate from Brno University of Technology, Czech Republic, where he is currently working towards the Ph.D. degree. In 2004, he was a visiting researcher at Aalborg University, Denmark, under the European Union exchange program Socrates/Erasmus. His research interests include computational electromagnetics with focus on the finite-difference time-domain method and its fast

and efficient implementation.

Mr. Franek is the recipient of the Seventh Annual SIEMENS Award for outstanding scientific publication.



Gert Frølund Pedersen was born in 1965. He received the B.Sc.E.E. degree, with honour, in electrical engineering from College of Technology in Dublin, Ireland, and the M.Sc.E.E. degree and Ph.D. from Aalborg University in 1993 and 2003. He has been employed by Aalborg University since 1993 where he currently is working as Professor for the Antenna and Propagation group. His research has focused on radio communication for mobile terminals including Antennas, Diversity systems, Propagation and Biological effects. He has also worked as consultant for developments of antennas for mobile terminals including the first internal antenna for mobile phones in 1994 with very low SAR, first internal triple-band antenna in 1998 with low SAR and high efficiency, small and highly efficient headset antenna in 2004 and various antenna diversity systems rated as the most efficient on the market.

Recently he has been involved in establishing a method to measure the communication performance for mobile terminals that has been used as basis for 2G and 3G standard where measurements also including the antenna are needed. The measurement technique is currently used in mobile terminals for beyond 3G terminals including several antennas to enhance the data communication. Further he is currently involved in several human biological studies investigating 3G-basestation, TETRA terminals and PET scanning of users of mobile phones.

He has been involved in establishing a method to measure the communication performance for mobile terminals that has been used as basis for 2G and 3G standard where measurements also including the antenna are needed. The measurement technique is currently used in mobile terminals for beyond 3G terminals including several antennas to enhance the data communication. Further he is currently involved in several human biological studies investigating 3G-basestation, TETRA terminals and PET scanning of users of mobile phones.



Jørgen Bach Andersen received the M.Sc. and Dr.Techn. degrees from the Technical University of Denmark (DTU), Lyngby, Denmark, in 1961 and 1971, respectively. In 2003 he was awarded an honorary degree from Lund University, Sweden. From 1961 to 1973, he was with the Electromagnetics Institute, DTU and since 1973 he has been with Aalborg University, Aalborg, Denmark, where he is now a Professor Emeritus.

He has been a Visiting Professor in Tucson, Arizona, Christchurch, New Zealand, Vienna, Austria, and Lund, Sweden. From 1993–2003, he was Head of the Center for Person-kommunikation (CPK), dealing with modern wireless communications. He has published widely on antennas, radio wave propagation, and communications, and has also worked on biological effects of electromagnetic systems. He was on the management committee for COST 231 and 259, a collaborative European program on mobile communications. He is presently on IEEE Electromagnetics Awards Committee.

Professor Andersen is a Life Fellow of IEEE and a former Vice President of the International Union of Radio Science (URSI) from which he was awarded the John Howard Dellinger Gold Medal in 2005.